Efficient Three-Dimensional Imaging Method Based on Enhanced Range Point Migration for UWB Radars

Shouhei Kidera, *Member, IEEE*, and Tetsuo Kirimoto, *Senior Member, IEEE*

***Abstract*—Ultrawideband pulse radar has a definite advantage over optical ranging techniques in harsh optical environments, such as a dark smog or strong backlight. In security or rescue situations with blurry visibility, it is particularly promising for identifying human bodies. One of the most promising approaches for this type of application is the recently proposed range point migration (RPM) method, which is beneficial for nonparametric imaging and is robust in noisy or heavy interference situations. However, the original RPM requires a discretization of the direction-of-arrival variables in its search operation. The resulting coarse discretization seriously degrades the imaging accuracy, particularly for 3-D problems and far-field observations. Consequently, in this approach, there is a major tradeoff between the amount of computation and accuracy. To overcome this difficulty, this letter proposes a more efficient RPM method, where the extraction of the point of intersection of spheres is adopted. A distinct advantage of this method is that the accuracy is basically invariant to the observation range when avoiding the aforementioned discretization. Numerical simulations including noisy cases prove that our proposed RPM significantly reduces the computation complexity while retaining imaging accuracy.**

***Index Terms*—Fast and accurate 3-D imaging, inverse problems, microwave imaging, radar signal processing, range point migration (RPM), ultrawideband (UWB) radar.**

I. Introduction

ULTRAWIDEBAND (UWB) pulse radar with high range resolution is promising for various sensing systems. A robotic or security sensor is one of the most promising applications of UWB radar, as it is able to identify a human body even in optically harsh environments, such as dark smog in disaster areas or high-density gas in resource exploration scenarios. It is also in demand for noncontact measurement in manufacturing such as reflector antennas or aircraft bodies requiring high-precision surfaces. Furthermore, it is suitable for the extraction of accurate surface images of the human breast in the early-stage breast cancer detection, where the artifact signal from the breast surface often causes severe interference when focusing on a tumor [1].

While various radar imaging methods have been developed based on aperture synthesis, time reversal approach [2], range migration [3], or genetic-algorithm-based solutions for domain integral equations [4], they are not practical for the aforementioned applications because it is generally hard to balance both low computation cost and high spatial resolution. To overcome the problem in the conventional techniques, a number of radar imaging methods for specifying clear surface extraction have been developed to attain an accuracy beyond a wavelength [6], [7]. Although these methods have been adopted for typical surface imaging applications, such as breast cancer detection [1] and through-the-wall imaging [8], they are only suitable in situations that are less noisy or less subject to interference.

As a high-speed and accurate 3-D imaging method applicable to cases with severe interference or noise, the range point migration (RPM) method has been established [9]. This method directly estimates an accurate direction of arrival (DOA) exploiting the global distribution of observed range points (a set of antenna locations and ranges), avoiding the difficulty of connecting them. A distinct advantage of this method is that it can accomplish high-speed and accurate 3-D imaging based on an entirely nonparametric (dealing with arbitrary shape) approach, where neither image pairing nor interpolation scheme is necessary. Another notable advantage of this method is that it offers superresolution imaging for quite complicated target shape including concave surface or edge region or multiple objects, where the frequency domain interferometer is adopted to enhance accuracy and resolution for the range extraction [10]. Because of this property, this method has been applied to various applications in recent years, such as complex-shape identification [11], shadow region imaging proactively employing a multiple scattering component [12], or the internal imaging for an embedded target surrounded by a dielectric medium with a complex-shaped surface [13], where the dielectric medium boundary can be accurately extracted by the RPM. However, this method has a unique drawback in that it requires fine discretization of the searching variables for the DOA, to obtain sufficient accuracy on the order of 1/100 wavelength.

In the case of a 3-D problem and far-field observation, this property generates a major tradeoff between the amount of computation and the imaging accuracy. As a significant solution to this problem, this letter newly proposes a point of intersection (PI)-extraction-based RPM method. In our proposed method, the spatial accumulation of the PIs, determined by the neighboring antenna locations and their ranges, is appropriately assessed. As a notable feature of this method, it completely resolves the aforementioned tradeoff by avoiding a fine discretization of the assumed variables. The numerical analysis employing the scattered data generated by the finite-difference time domain (FDTD) method demonstrates that our improved RPM method dramatically reduces the amount of computation

Manuscript received April 8, 2012; revised August 27, 2012, October 1, 2012, November 7, 2012, and November 11, 2012; accepted November 23, 2012. Date of publication January 23, 2013; date of current version June 13, 2013.

The authors are with the Graduate School of Informatics and Engineering, The University of Electro-Communications, Chofu 182-8585, Japan (e-mail: kidera@ee.uec.ac.jp; kirimoto@ee.uec.ac.jp).

Color versions of one or more of the figures in this paper are available online at http://ieeexplore.ieee.org.

Digital Object Identifier 10.1109/LGRS.2012.2230611

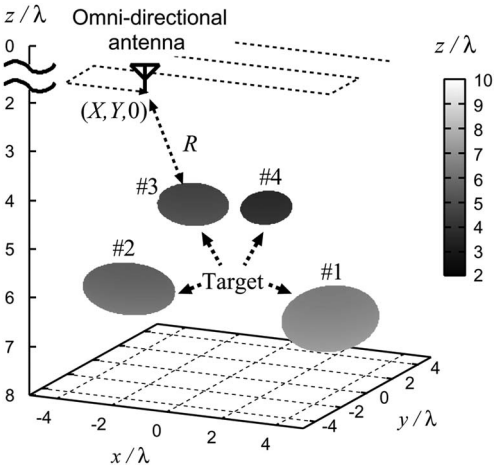

Fig. 1. System model in 3-D problem.

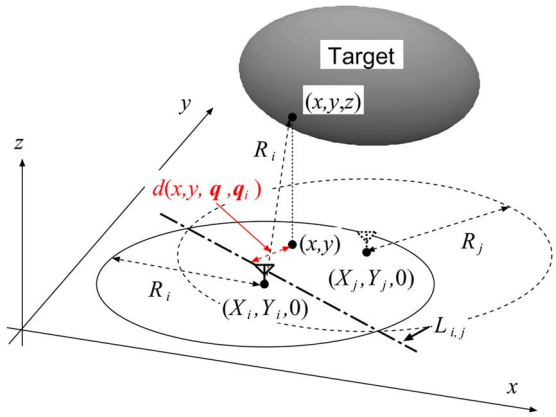

Fig. 2. Spatial relationship among two circles, intersection line, and distance $d(x, y, \boldsymbol{q}_i, \boldsymbol{q}_j)$.

and enhances the accuracy of target surface extraction, even in noisy situations.

II. System Model

Fig. 1 shows the system model. It assumes the monostatic radar, and an omnidirectional antenna is scanned on $z = 0$ plane. It is assumed that the target has an arbitrary shape including concave surface or edge region and has a clear boundary, namely, the spatial gradient of conductivity or permittivity around its boundary is expressed as Dirac's delta function [5], where its contrast value should be sufficiently high to obtain a high reflection echo from the target boundary. This is a significant condition for achieving accurate target boundary extraction using the proposed method in this study. In general indoor sensing issues, an assumed object such as human body (with skin surface), furniture, or wall can satisfy this clear boundary condition. The propagation speed of the radio wave c is assumed to be a known constant. A monocycle pulse is used as the transmitting current, whose central wavelength is defined as λ. The real space, in which the target and antenna are located, is expressed by the parameters (x, y, z). $z > 0$ is assumed for simplicity. $s'(\boldsymbol{q})$ with $\boldsymbol{q} = (X, Y, R)$ is defined as the scattered electric field received at the antenna location $(x, y, z) = (X, Y, 0)$, where $R = ct/2$ is a function of time t. $s(\boldsymbol{q})$ is defined as the output of the Wiener filter with the transmitted waveform, the detail of which is described in [9]. A set of antenna locations and ranges as $\boldsymbol{q}$, called a range point, is extracted from the local maxima of $s(\boldsymbol{q})$.

III. Conventional RPM Method

There are various imaging methods for near-field or far-field sensing, as described in Section I. The RPM method has been proposed as a promising approach applicable to various 3-D target shapes such as concave surface and edge ridges with 1/100 wavelength accuracy [9]. This method is based on the assumption that a target boundary point (x, y, z) exists on a sphere with its center as the antenna location $(X, Y, 0)$ and its radius as the observed range R. The DOA, such as the azimuth and elevation angles, is transformed to variables (x, y) for simplicity, which are determined by assessing the spatial accumulation of intersecting circles between the spheres, determined by one $\boldsymbol{q}_i$ and another $\boldsymbol{q}_j$. Each intersecting circle projected to a scanning plane becomes a line defined as $L_{i,j}$. This method determines the target location (x, y) by evaluating the degree of integration of the intersection lines as

$$(x(\boldsymbol{q}_i), y(\boldsymbol{q}_i)) = \arg\max_{(x,y)} \sum_{j=1}^{N_q} f(\boldsymbol{q}_i, \boldsymbol{q}_j) \times \exp\left\{-\frac{d(x, y, \boldsymbol{q}_i, \boldsymbol{q}_j)^2}{2\sigma_d^2}\right\} \quad (1)$$

$$f(\boldsymbol{q}_i, \boldsymbol{q}_j) = s(\boldsymbol{q}_j) \exp\left\{-\frac{D(\boldsymbol{q}_i, \boldsymbol{q}_i)^2}{2\sigma_D^2}\right\} \quad (2)$$

where $d(x, y, \boldsymbol{q}_i, \boldsymbol{q}_j)$ denotes the minimum distance between the projected line $L_{i,j}$ and $(x, y, 0)$. Fig. 2 shows the spatial relationship among the circles and its intersection line. $D(\boldsymbol{q}, \boldsymbol{q}_i) = \sqrt{(X - X_i^2) + (Y - Y_i^2)}$, σ_d, and σ_D are empirically determined based on the criteria described in [9]. Under the assumption $z \geq 0$, the z coordinate of each target point is given by $z(\boldsymbol{q}_i) = \sqrt{R_i^2 - \{x(\boldsymbol{q}_i) - X_i\}^2 - \{y(\boldsymbol{q}_i) - Y_i\}^2}$. Note that false target points caused by the random noises are removed by assessing the evaluation value in the right term of (2) as in [9]. This method does not require the connecting procedures of a large number of range points and produces accurate target points, even if an extremely complicated range map is given. This characteristic is described in detail in [9].

Its only drawback is that a sufficiently dense discretization for (x, y) is required to obtain the desired accuracy beyond a wavelength. In addition, it is predicted that fine sampling will considerably increase the amount of computation required to calculate (2), resulting in a compromise between the required computational amount and the attained accuracy, particularly in longer range observations.

IV. Proposed RPM Method

As a significant solution to the aforementioned problem, this letter proposes a quick and accurate enhanced RPM method. This method is on the basis that the actual target boundary point

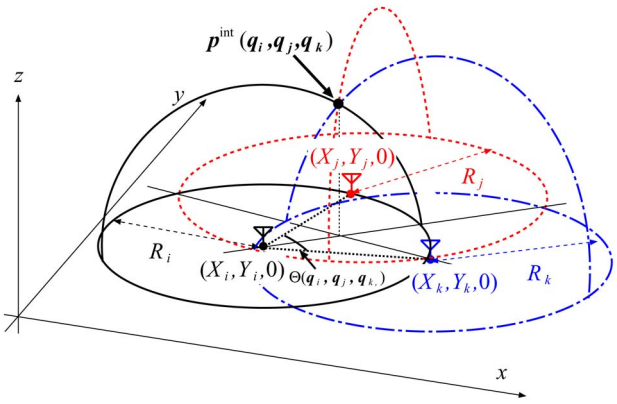

Fig. 3. Relationship among three spheres determined by $\boldsymbol{q}_i$, $\boldsymbol{q}_j$, $\boldsymbol{q}_k$, and its PI.

should be included in all the possible PIs determined by the neighboring range points. Instead of searching the discretized DOA variables, this method then extracts an optimal PI by assessing the spatial accumulation of PIs. That is, this method determines the target point for range point $\boldsymbol{q}_i$ as

$$\hat{\boldsymbol{p}}(\boldsymbol{q}_i) = \underset{\boldsymbol{p}^{\mathrm{int}}(\boldsymbol{q}_i;\boldsymbol{q}_l,\boldsymbol{q}_m)\in\mathcal{P}_i}{\arg\max} \sum_{(\boldsymbol{q}_j,\boldsymbol{q}_k)\in\mathcal{Q}_i} g(\boldsymbol{q}_i;\boldsymbol{q}_j,\boldsymbol{q}_k) \times \exp\left\{-\frac{\left\|\boldsymbol{p}^{\mathrm{int}}(\boldsymbol{q}_i;\boldsymbol{q}_j,\boldsymbol{q}_k)-\boldsymbol{p}^{\mathrm{int}}(\boldsymbol{q}_i;\boldsymbol{q}_l,\boldsymbol{q}_m)\right\|^2}{2\sigma_r^2}\right\} \quad (3)$$

where $\boldsymbol{p}^{\mathrm{int}}(\boldsymbol{q}_i;\boldsymbol{q}_j,\boldsymbol{q}_k)$ denotes the PI among the three spheres, determined by the range points $\boldsymbol{q}_i$, $\boldsymbol{q}_j$, and $\boldsymbol{q}_k$, and σ_r is an empirically determined constant. Note that, in determining σ_r, the spatial density of the accumulated PI should be considered. In general, it should be smaller than the interval between scanning samples because a sparse sampling of antenna scanning generates a sparse distribution of PIs. Fig. 3 presents the spatial relationship between the three spheres with $\boldsymbol{q}_i$, $\boldsymbol{q}_j$, $\boldsymbol{q}_k$, and its PI. The weighting function $g(\boldsymbol{q}_i;\boldsymbol{q}_j,\boldsymbol{q}_k)$ is defined by

$$g(\boldsymbol{q}_i;\boldsymbol{q}_j,\boldsymbol{q}_k) = f(\boldsymbol{q}_i,\boldsymbol{q}_j) + f(\boldsymbol{q}_i,\boldsymbol{q}_k) \quad (4)$$

which yields the convergence effect of PIs with respect to the antenna locations, similar to the original RPM [9]. To enhance the optimization speed in (3), this method narrows down the investigating region of antenna locations and PIs, using

$$\mathcal{Q}_i = \left\{(\boldsymbol{q}_j,\boldsymbol{q}_k)\middle| D(\boldsymbol{q}_i,\boldsymbol{q}_j)\le\sigma_D, D(\boldsymbol{q}_i,\boldsymbol{q}_k)\le\sigma_D, \Theta(\boldsymbol{q}_i,\boldsymbol{q}_j,\boldsymbol{q}_k)\le\epsilon_{\mathrm{n}}\right\} \quad (5)$$

$$\mathcal{P}_i = \left\{\boldsymbol{p}^{\mathrm{int}}(\boldsymbol{q}_i;\boldsymbol{q}_j,\boldsymbol{q}_k)\middle|(\boldsymbol{q}_j,\boldsymbol{q}_k)\in\mathcal{Q}_i\right\} \quad (6)$$

where $\Theta(\boldsymbol{q}_i,\boldsymbol{q}_j,\boldsymbol{q}_k) = ((X_i-X_j)(X_i-X_k)+(Y_i-Y_j)(Y_i-Y_k))/\{D(\boldsymbol{q}_i,\boldsymbol{q}_j)D(\boldsymbol{q}_i,\boldsymbol{q}_k)\}$ measures an orthogonality among the three antenna locations as in Fig. 3. To enhance the imaging accuracy, the range points are selected so that the position relationship of each antenna location satisfies an orthogonal relationship, and $\epsilon_n \ll 1$ should be then set in (5), which should also depend on the spatial arrangement of antenna scanning. Here, similar to the conventional method, false target points due to random noises are eliminated by assessing the evaluation value in the right term of (3). This method does not need enormous sampling of the searching variables for the DOA but extracts an appropriate PI from possible PIs. Then, the imaging accuracy of this method is essentially impervious to the discretization intervals of DOA variables and completely resolves the tradeoff existing in the conventional RPM method.

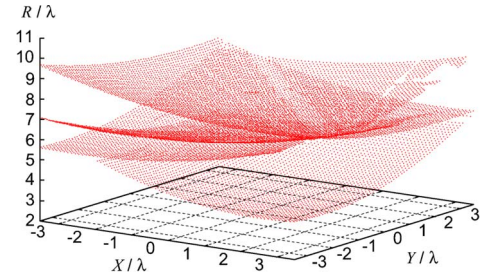

Fig. 4. Extracted range points in assuming the case in Fig. 1.

In addition, this method does not need to narrow the investigation area about the imaging region to achieve numerical efficiency for 3-D imaging because our method exploits the spatial distribution of PIs, which can be directly determined by the three spheres defined by the three range points. The actual target boundary should be located around the accumulated spatial region of these PIs. *A priori* information about an object's shape or location is not then needed in the proposed method, while the conventional method must adopt the narrowing scheme of the imaging region (x, y) as in (2) to reduce the amount of calculation. This is a substantial advantage of the proposed method.

V. Performance Evaluation in Numerical Simulation

This section describes the numerical-simulation-based evaluations for the conventional and proposed RPM methods. The monostatic radar is scanned for $-3.5\lambda \le x, y \le 3.5\lambda$, where the number of locations on each axis is 71. The four elliptical objects of different sizes are placed as in Fig. 1. Here, each elliptical object has a homogeneous medium and satisfies the clear boundary condition as mentioned in Section II, where the conductivity is 1.0×10^6 S/m and the relative permittivity is 1.0. The received signals in each antenna location $s(\boldsymbol{q})$ are generated by the FDTD method. Fig. 4 shows a 3-D view of the range points extracted from $s(\boldsymbol{q})$, which are distributed as a multivalued function for the antenna location, corresponding to situations with rich interference. All of these range points are collectively handled by the conventional or the proposed RPM methods, so the interference effects between multiple objects are naturally considered in this simulation.

The left side of Fig. 5 illustrates the 3-D zoom-up images and its cross-sectional views at $|x-2.5\lambda\le0.05\lambda$ and $|y+2.5\lambda|\le0.05\lambda$ for #4 (smallest) target, obtained by the conventional RPM, where the discretization interval Δs of (x, y) used in (2) is 0.25λ, i.e., the coarsely sampled case in the conventional method. Here, $\sigma_D = 0.5\lambda$ and $\sigma_d = 0.1\lambda$ are set. The calculation amount in this case is 300 s, using a Xeon 3.2-GHz processor. This result demonstrates that the 3-D image obtained is degraded from the actual target boundary, because the discretized interval is not small enough to express the elliptical surfaces. This property is distinct in the smaller

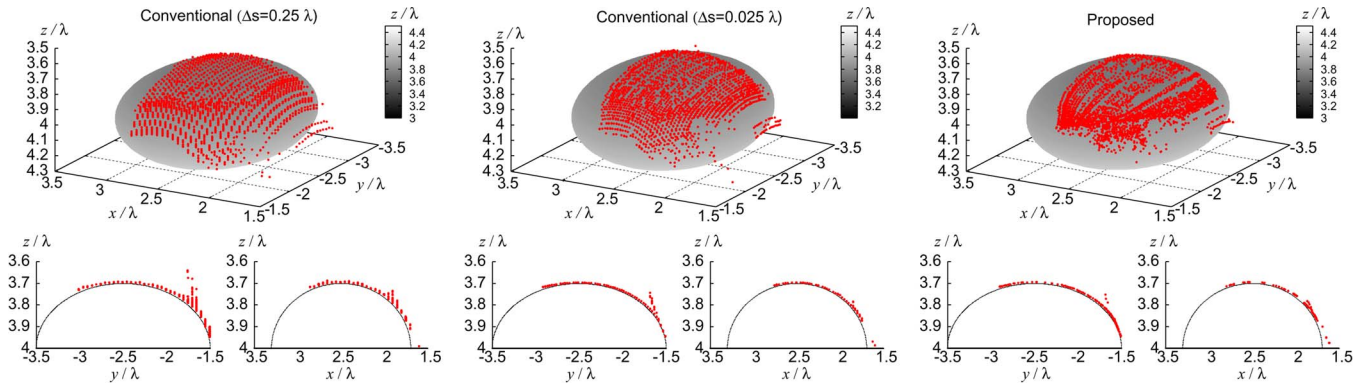

Fig. 5. (Left, top) Three-dimensional image and its cross-sectional views at (left, bottom left) $|x - 2.5\lambda| \leq 0.05\lambda$ and (right, bottom right) $|y + 2.5\lambda| \leq 0.05\lambda$ obtained by the conventional method for #4 target, in the case of coarse sampling as $\Delta s = 0.25\lambda$. (Middle) Obtained by the conventional method for #4 target, in the cose of dense sampling as $\Delta s = 0.025\lambda$. (Right) Obtained by the proposed method for #4 target.

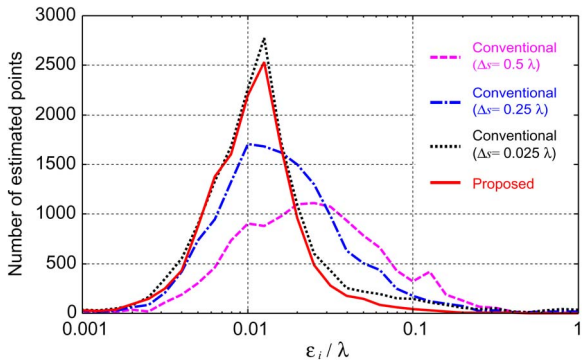

Fig. 6. Error distribution for each method.

target case as in Fig. 5 (left). As the densely sampled case in the conventional method, the middle of Fig. 5 presents the same view as in the left side for #4 target, where Δs is set to 0.025λ. This result shows that the images obtained more accurately express the target surface because of dense discretization. However, this requires more than 16 200 s (4.5 h) to obtain the 3-D image, which is impractical for likely applications, such as robotics or security sensors. Moreover, this result is affected by the discretized error for the 3-D image obtained, particularly in the case of the small target as in Fig. 5 (middle).

On the contrary, the right side of Fig. 5 shows the same view as in the left side obtained by the proposed method for #4 target case, where $\sigma_D = 0.5\lambda$, $\sigma_r = 0.05\lambda$, and $\epsilon_n = 0.01$ are set. The calculation amount in this case is 250 s, using the previous processor. This result confirms that our method greatly enhances the imaging accuracy without increasing the amount of computation. It is notable that this method avoids the discretization error from searching for the DOA and completely resolves the tradeoff in the conventional RPM method.

Furthermore, as a quantitative analysis, the following amount ϵ_i is defined as:

$$\epsilon_i = \min_{\boldsymbol{p}_{\rm true}} \left\| \boldsymbol{p}_{\rm true} - \boldsymbol{p}_e^i \right\|, \quad (i = 1, 2, \ldots, N_T) \tag{7}$$

where $\boldsymbol{p}_{\rm true}$ and $\boldsymbol{p}_e^i$ express the locations of the true and estimated target points, respectively. N_T is the total number of $\boldsymbol{p}_e^i$. Fig. 6 shows the number of target points for each accuracy ϵ_i, where the discretization interval is varied in the conventional method. This figure shows that ϵ_i of the proposed method accumulates to around the order of 1/100 of a wavelength, which is almost the same as the accuracy for the most densely sampled cases using the conventional method. The imaging error of the proposed method caused by the interference effect from the other objects because of finite range resolution and the waveform deformation owing to frequency dependence of boundary scattering at a wavelength size object should be noted [10]. Moreover, in the case of an inhomogeneous medium, it is considered that the imaging accuracy will be more degraded because more deformation of the scattering waveform is caused by the frequency dependence of the local reflection coefficient, which depends on an internal dielectric structure underneath the target surface.

Finally, the situation in a noisy case is investigated, where white Gaussian noise is added to the received signals $s(\boldsymbol{q})$. In this case, the S/N is set to 30 dB, which can be accomplished in the far-field UWB radar systems, experimentally realized in [10]. The left and middle of Fig. 7 present the same views as in Fig. 5 obtained by the conventional RPM method for the #4 target, in the case of $\Delta s = 0.25\lambda$ and $\Delta s = 0.025\lambda$, respectively. Both figures show that there are small fluctuations due to random noisy components when compared to noiseless situations, but these are not a fatal degradation in accuracy, which is a notable feature of the original RPM. In addition, the right side of Fig. 7 shows the same views as in Fig. 5 obtained by the proposed method in the situation described earlier. As to false image reduction due to noisy component, the thresholds with respect to (2) and (3) are set to the same values. This figure demonstrates that the estimated target points can correctly express the elliptic target surface, while a small accuracy degradation appeared as occurred in the conventional method. Furthermore, Fig. 8 presents the number of target points with the error ϵ_i for each method, in the noisy case. This evaluation quantitatively demonstrates that the proposed method holds a robustness to random noise fluctuation as good as the original RPM method.

VI. Conclusion

This letter has newly proposed the efficient 3-D imaging method based on RPM, for far-field sensing techniques. The

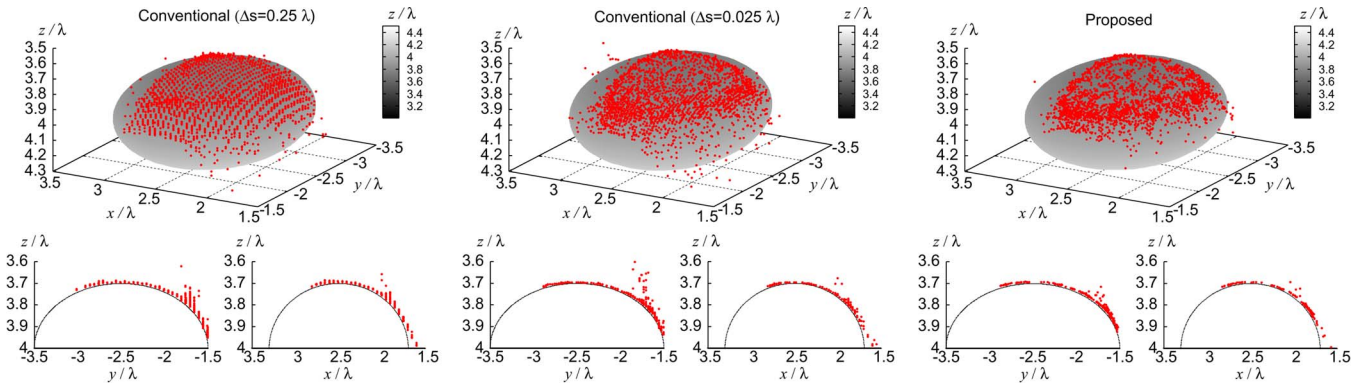

Fig. 7. Same view as in Fig. 5 obtained by (left) the conventional method for #4 target, in the case of coarse sampling as $\Delta s = 0.25\lambda$ in noisy situation, (middle) by the conventional method for #4 target, in the case of dense sampling as $\Delta s = 0.025\lambda$ in noisy situation, and (right) obtained by the proposed method for #4 target in noisy situation.

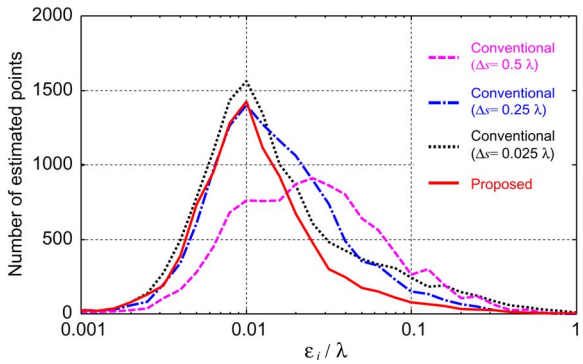

Fig. 8. Error distribution for each method in noisy situation.

original RPM has the drawback that its imaging accuracy greatly depends on the discretization size of the searching variables for the DOA, and there is an unresolvable tradeoff between the amount of computation required and the imaging accuracy. To counter this difficulty, this letter switched the imaging process in the RPM method, where the optimal PI is extracted from all the possible PIs determined by the neighboring range points, by evaluating their degree of spatial accumulation. Numerical validations verified that our improved RPM method completely answers the tradeoff with the conventional RPM and, under the FDTD simulation, it can obtain around 1/100 wavelength accuracy without increasing the amount of computation. Finally, the investigation in a noisy situation demonstrated that this method is as robust as the original RPM.

REFERENCES

[1] D. W. Winters, J. D. Shea, E. L. Madsen, G. R. Frank, B. D. Van Veen, and S. C. Hagness, "Estimating the breast surface using UWB microwave monostatic backscatter measurements," *IEEE Trans. Biomed. Eng.*, vol. 55, no. 1, pp. 247–256, Jan. 2008.

[2] D. Liu, J. Krolik, and L. Carin, "Electromagnetic target detection in uncertain media: Time-reversal and minimum-variance algorithms," *IEEE Trans. Geosci. Remote Sens.*, vol. 45, no. 4, pp. 934–944, Apr. 2007.

[3] F. Soldovieri, A. Brancaccio, G. Prisco, G. Leone, and R. Pieri, "A Kirchhoff-based shape reconstruction algorithm for the multimonostatic configuration: The realistic case of buried pipes," *IEEE Trans. Geosci. Remote Sens.*, vol. 46, no. 10, pp. 3031–3038, Oct. 2008.

[4] A. Massa, D. Franceschini, G. Franceschini, M. Pastorino, M. Raffetto, and M. Donelli, "Parallel GA-based approach for microwave imaging applications," *IEEE Trans. Antennas Propag.*, vol. 53, no. 10, pp. 3118–3127, Oct. 2005.

[5] T. Sakamoto and T. Sato, "A target shape estimation algorithm for pulse radar systems based on boundary scattering transform," *IEICE Trans. Commun.*, vol. E87-B, no. 5, pp. 1357–1365, May 2004.

[6] T. Sakamoto, "A fast algorithm for 3-dimensional imaging with UWB pulse radar systems," *IEICE Trans. Commun.*, vol. E90-B, no. 3, pp. 636–644, Mar. 2007.

[7] S. Kidera, T. Sakamoto, and T. Sato, "High-resolution and real-time three-dimensional imaging algorithm with envelopes of spheres for UWB radars," *IEEE Trans. Geosci. Remote Sens.*, vol. 46, no. 11, pp. 3503–3513, Nov. 2008.

[8] S. Hantscher, A. Reisenzahn, and C. G. Diskus, "Through-wall imaging with a 3-D UWB SAR algorithm," *IEEE Signal Process. Lett.*, vol. 15, no. 1, pp. 269–272, Feb. 2008.

[9] S. Kidera, T. Sakamoto, and T. Sato, "Accurate UWB radar 3-D imaging algorithm for complex boundary without range points connections," *IEEE Trans. Geosci. Remote Sens.*, vol. 48, no. 4, pp. 1993–2004, Apr. 2010.

[10] S. Kidera, T. Sakamoto, and T. Sato, "Super-resolution UWB radar imaging algorithm based on extended capon with reference signal optimization," *IEEE Trans. Antennas Propag.*, vol. 59, no. 5, pp. 1606–1615, May 2011.

[11] R. Salman and I. Willms, "3D UWB radar super-resolution imaging for complex objects with discontinuous wavefronts," in *Proc. IEEE Int. Conf. Ultra Wideband*, Sep. 2011, pp. 346–350.

[12] S. Kidera and T. Kirimoto, "Fast and shadow region 3-dimensional imaging algorithm with range derivative of doubly scattered signals for UWB radars," *IEEE Trans. Antennas Propag.*, vol. 60, no. 2, pp. 984–996, Feb. 2012.

[13] K. Akune, S. Kidera, and T. Kirimoto, "Accurate and nonparametric imaging algorithm for targets buried in dielectric medium for UWB radars," *IEICE Trans. Electron.*, vol. E95-C, no. 8, pp. 1389–1398, Aug. 2012.